MR scanner independent 3D B_1 field mapping of magnetic resonance spectroscopy RF coils using an automated measurement system

Vaclav Brandejsky

MR scanner independent 3D B_1 field mapping of magnetic resonance spectroscopy RF coils using an automated measurement system

Examensarbete utfört vid
Tekniska högskolan i Linköping
av

Vaclav Brandejsky

LITH-IMT/BIT30-A-EX--08/469—SE

Handledare: **Olof Dahlquist Leinhard**
                IMH, Linköpings universitet

Examinator: **Peter Lundberg**
                IMH, Linköpings universitet

Linköping, 22 August, 2008

	Linköpings tekniska högskola Institutionen för medicinsk teknik	Rapportnr: LITH-IMT/BIT30-A-EX--08/469--SE Datum: 2008-08-22

Svensk titel	Magnetkameraoberoende bestämning av 3D vektor B_1-fält av magnetkameraspolar med ett automatiserat mätsystem
Engelsk titel	MR scanner independent 3D B_1 field mapping of magnetic resonance spectroscopy RF coils using an automated measurement system
Författare	Vaclav Brandejsky

Uppdragsgivare: Radiofysik, LiO	Rapporttyp: Examensarbete	Rapportspråk Engelska

Sammanfattning
Abstract

Radiofrekventa - spolars känslighetsmönster är viktigt för avbildning med magnetkamera (MRI) och magnetresonansspektroskopi (MRS). Vetskap om RF-spolars känslighet för och förmåga att skapa RF-magnetfält ($\mathbf{B}_1$) kan användas för att åstadkomma korrekta excitationsflipvinklar och för att korrigera uppmätta signalstyrkor. Det är också viktigt för att göra MRI och MRS undersökningar snabbare och för att förbättra kvalitén på rekonstruerade bilder. Vi har utvecklat en metod för mätning av $\mathbf{B}_1^-$ och $\mathbf{B}_1^+$ fält i en testbänk som alternativ till metoder där $\mathbf{B}_1$ fältet bestäms inne i magnetkameran. Uppställningen omfattar ett industriellt koordinatbord kontrollerat av PC-baserade program, sökspolar för detektion av $\mathbf{B}_1$ fält, en tvåports nätverksanalysator och ett analog till digital omvandlingskort. Mätningen är möjlig att utföra i olika vätskor, exempelvis saltlösning, för att efterlikna olika former och dielektriska egenskaper hos människokroppen.

Knowledge about the magnetic field distribution in radio frequency coils is important for both magnetic resonance imaging and magnetic resonance spectroscopy. The information about the field's distribution is used to obtain correct excitation pulse flip angles, as well as to perform signal strength corrections. Another use is also accelerating imaging and spectroscopic examinations, where accurate definition of the $\mathbf{B}_1^-$ field is essential to perform proper image and/or spectrum reconstruction.

We developed a method for measurement of the $\mathbf{B}_1^-/\mathbf{B}_1^+$ fields as an alternative approach to $\mathbf{B}_1^-/\mathbf{B}_1^+$ fields assessment in MR scanner. Our setup incorporates an industrial coordinate table controlled by a PC-based program, search coils, a two-port vector network analyzer and an analog-to-digital (A/D) card. It is possible to measure in various liquid media (for example in saline solution) to mimic different shapes and dielectric properties of the human body.

Nyckelord:
Keywords
RF coil, MRS, NMR, spectroscopy

Bibliotekets anteckningar:

Abstract

Knowledge about the magnetic field distribution in radio frequency coils is important for both magnetic resonance imaging and magnetic resonance spectroscopy. The information about the field's distribution is used to obtain correct excitation pulse flip angles, as well as to perform signal strength corrections. Another use is also accelerating imaging and spectroscopic examinations, where accurate definition of the $\mathbf{B}_1^-$ field is essential to perform proper image and/or spectrum reconstruction.

We developed a method for measurement of the $\mathbf{B}_1^-/\mathbf{B}_1^+$ fields as an alternative approach to $\mathbf{B}_1^-/\mathbf{B}_1^+$ fields assessment in MR scanner. Our setup incorporates an industrial coordinate table controlled by a PC-based program, search coils, a two–port vector network analyzer and an analog-to-digital (A/D) card. It is possible to measure in various liquid media (for example in saline solution) to mimic different shapes and dielectric properties of the human body.

Sammanfattning

Radiofrekventa - spolars känslighetsmönster är viktigt för avbildning med magnetkamera (MRI) och magnetresonansspektroskopi (MRS). Vetskap om RF-spolars känslighet för och förmåga att skapa RF-magnetfält ($\mathbf{B}_1$) kan användas för att åstadkomma korrekta excitationsflipvinklar och för att korrigera uppmätta signalstyrkor. Det är också viktigt för att göra MRI och MRS undersökningar snabbare och för att förbättra kvalitén på rekonstruerade bilder. Vi har utvecklat en metod för mätning av $\mathbf{B}_1^-$ och $\mathbf{B}_1^+$ fält i en testbänk som alternativ till metoder där $\mathbf{B}_1$ fältet bestäms inne i magnetkameran. Uppställningen omfattar ett industriellt koordinatbord kontrollerat av PC-baserade program, sökspolar för detektion av $\mathbf{B}_1$ fält, en tvåports nätverksanalysator och ett analog till digital omvandlingskort. Mätningen är möjlig att utföra i olika vätskor, exempelvis saltlösning, för att efterlikna olika former och dielektriska egenskaper hos människokroppen.

Acknowledgments

I would like to thank all the nice people at the Department of Radiation Physics and at CMIV in Linköping. I am grateful to Peter Lundberg and Eva Lund for giving me the opportunity to work at the MR department, Göran Salerud for helping me with the administrative tasks and Olof Dahlquist Leinhard for patience during our discussions over the project. I also have to thank to all my colleagues, mainly Anders and Mattias, for accepting me and helping me during the hard times of the project. Last but not least I would like to thank my parents, Jana and Milos, for supporting me.

Thank you!

Contents

Abbreviations and symbols

Abbreviations

A/D	analog to digital
AP	anterior-posterior direction
ATP	adenosine-triphosphate
CC	feet-head direction (Philips convention)
CNC	computer numerical control
DMMP	dimethyl methylphosphonate
EM	electromagnetic
FH	feet-head direction
GPIB	general purpose interface bus
MOS	metal oxide semiconductor
MRI	magnetic resonance imaging
MR	magnetic resonance
MRS	magnetic resonance spectroscopy
NC	numerical control
NMR	nuclear magnetic resonance
PC	phosphocholine
PDE	phosphodiester
Pi	inorganic phosphate
PLC	programmable logic controller
PME	phosphomonoester

RAM   random access memory

RF   radio frequency

RL   right-left direction

SNR   signal-to-noise ratio

TTL   transistor-transistor logic

VOI   volume of interest

Symbols

$\mathbf{B}$ [T]   magnetic field

ρ [$\Omega \cdot$ m]   resistivity

$\mathbf{E}$ [V/m]   electric field

ϵ [F/m]   permitivity

γ [rad/T/s]   gyromagnetic ratio

j complex unit

$\mathbf{J}$ [A/m^2]   current density

$\mathbf{M}$ transformation matrix

n [mol]   amount of substance

μ [H/m]   permeability

∇ nabla

$\partial/\partial t$ [$-$]   partial derivative in time

$\mathbf{R}$ rotation matrix

$\mathbf{T}$ translation matrix

t [s]   time

Chapter 1

Introduction

Exact knowledge about the $\mathbf{B}_1$ field associated with radio frequency (RF) coils used for signal transmission and reception in absolutely quantified MR spectroscopy is of major importance in order to compensate for its inhomogeneities. The transmission $\mathbf{B}_1$ field (often referred to as the $\mathbf{B}_1^+$ field) is important in order to obtain correct excitation pulse flip angles, as well as for reciprocity based signal strength corrections. The receiving $\mathbf{B}_1$ field ($\mathbf{B}_1^-$) is then used to perform signal strength corrections and also to accelerate both imaging and spectroscopic examinations, where accurate definition of the $\mathbf{B}_1^-$ field is essential to perform proper image and/or spectrum reconstruction. It is now widely accepted, that the *Principle of reciprocity* applies to MR phenomena in addition to classical *Antenna reciprocity theorem* [1, 2]. The Principle states that the sensitivity of an RF coil used as a receiver to nuclei located at point X is proportional to that coil's efficiency when used as a transmitter to generate a RF field $\mathbf{B}_1$ at the position X [2]. In other words, RF coil's electromagnetic (EM) field distribution remains the same independent on whether the coil serves as a receiver or transmitter [1].

Several MR scanner based strategies of the $\mathbf{B}_1$ field analysis already exist (for example [3, 4]). These methods use fantoms and sophisticated imaging sequences to estimate the $\mathbf{B}_1$ field distribution. Because the complexity of coil design used in MR experiments increases and since it is often difficult to perform MR scanner based mapping of the associated RF field, there is need for scanner independent methods of $\mathbf{B}_1^-/\mathbf{B}_1^+$ field mapping. The obvious solution for these MR independent methods could be computer simulation of the RF field based on Maxwell's equations and the Biot-Savart law using finite element computations. However, the physical complexities of coil arrays and more or less arbitrary shaped coils as well as anatomies affecting the $\mathbf{B}_1$ field often makes these simulations very difficult to perform and major simplifications in the simulation are required.

As an alternative approach we try to develop a measurement setup for direct measurement of the $\mathbf{B}_1^-/\mathbf{B}_1^+$ fields. Previously at the department a similar method was created, but compared to ours it was much simpler and less accurate [5]. The

setup incorporates an industrial coordinate table controlled by a PC-based program, a set of search coils, a two port vector network analyzer and an analog-to-digital (A/D) card. We believe the advantage of this setup is the ability to measure all vector components of the RF field in a realistic way, unaffected by limitations such as low SNR or specific Larmor frequencies which come up when performing MR experiments. The phase of the signal can also be obtained which is a huge advantage compared to methods nowadays available. Furthermore, it is possible to measure in various liquid media (for example in saline solution) to mimic different dielectric properties. Last but not least, the proposed method is relatively affordable, since most of the equipment can usually be found in laboratories involved in this area.

1.1 Specific aims

The aim of this master thesis is to create a setup allowing measurements of the $\mathbf{B}_1^-/\mathbf{B}_1^+$ fields, validate its functionality and to perform initial experiments where $\mathbf{B}_1$ field maps are created using the equipment.

More in detail, the work on the thesis involves finding out possibilities of electromagnetic field mapping and, based on the result of this literature search, setting up and programming the coordinate table and the vector network analyzer. Reliability of their cooperation must be assured because it will be essential for automatic mapping process. Furthermore, a function for registration of measured $\mathbf{B}_1$ field maps against MR visible markers attached to used RF coil will be designed and implemented. However, to be able perform this task principles of magnetic resonance spectroscopy and imaging must be investigated. All proposed methods of steering and mapping must be validated to assure stable results since we plan to use the method in the future in absolute quantification of metabolites in MRS.

Chapter 2

Theoretical background

In this chapter the theoretical background of this thesis will be presented. The reader will first be introduced to the basics of electromagnetism and the reciprocity principle, which both serve as the basis for future work. In the second part the magnetic resonance phenomenon will be shortly explained considering the focus of this thesis.

2.1   Electromagnetic field theory

Due to the nature of the thesis which concerns mapping of radio frequency (RF) fields and nuclear magnetic resonance (NMR), a brief introduction to the area of electromagnetic field theory needs to be given in this section. The main focus is on the relations between electric and magnetic fields. Ways of assessing the magnetic field distribution in space will be summarized.

Sometimes both **B** and **H** quantities are referred to as magnetic field; in order to avoid confusion we should clarify that when talking about magnetic field we mean the magnetic flux density **B**. The relation between **B** and **H** is given as [6]

$$\mathbf{H} = \frac{1}{\mu_0}\mathbf{B} \tag{2.1}$$

where $\mu_0 = 4\pi \cdot 10^{-7}$ is the permeability of free space.

2.1.1   Maxwell's equations

Maxwell's equations define relations between electric field, magnetic field and electric charge and current. These four equations in differential form follow [6]

$$\nabla \times \mathbf{E} = -\frac{\partial \mathbf{B}}{\partial t} \tag{2.2}$$

Equation (2.2) is known as the *Faraday's law* and states that a changing magnetic field **B** induces an electric field **E** with non-zero curl. The electric field's amplitude

is proportional to the change of the magnetic field. The nabla operator ∇ is, in three-dimensional Cartesian space, defined as $\nabla = \hat{\mathbf{x}}\frac{\partial}{\partial x} + \hat{\mathbf{y}}\frac{\partial}{\partial y} + \hat{\mathbf{z}}\frac{\partial}{\partial z}$, where $(\hat{\mathbf{x}},\hat{\mathbf{y}},\hat{\mathbf{z}})$ is the standard basis in $\Re^3$.

$$\nabla \times \mathbf{B} = \mu_0 \mathbf{J} + \mu_0 \epsilon_0 \frac{\partial \mathbf{E}}{\partial t} \tag{2.3}$$

The second equation is known as *Ampère's circuital law* [6] and relates current flowing through a closed loop with magnetic field around that loop (where μ_0 is permeability, ϵ_0 is dielectric constant and $\mathbf{J}$ current density). The last term in eq. (2.3) is called displacement current and reflects the time variance of the electric field.

$$\nabla \cdot \mathbf{E} = \frac{\rho}{\varepsilon_0} \tag{2.4}$$

$$\nabla \cdot \mathbf{B} = 0 \tag{2.5}$$

Equation (2.4) is *Gauss's law* for $\mathbf{E}$ [6]. It states that electric flux of the electric field $\mathbf{E}$ over closed surface is equal to the total charge enclosed. Equation (2.5),which has no particular law assigned to it, disallows a magnetic monopole.

To summarize the impact of Maxwell's equations:

1. All time varying magnetic fields give rise to electric fields and vice versa [6]; this fact serves as the basis of detection of a NMR signal.

2. A current flowing through a conductor generates magnetic field around that conductor.

2.1.2 Biot-Savart law

We have now introduced Maxwell's equations which describe relations between electric and magnetic fields and show why magnetic resonance effects can be induced and measured (more detail on magnetic resonance phenomena can be found in section 2.1.3) using RF coils.

Ampere's law can in praxis be used to create EM field by applying electrical current to a conductor. However, since the Ampère's law can directly be applied only in cases where some symmetry is present [6] (for example for infinitely long wire or solenoid), another solution has to be used for e.g. single loop coils where the length of the conductor is finite. In these cases the law cannot be used to asses the distribution, or shape, of the induced magnetic field $\mathbf{B}$. It can, however, be assessed by the *Biot-Savart law* [6], which states that magnetic field $\mathbf{B}$ in point P can be obtained by summing elementary contributions $d\mathbf{B}$ from differential loop element $d\mathbf{l}$. The elementary contribution is expressed in eq. (2.6) [6]

$$d\mathbf{B} = \frac{\mu_0 I\left(d\mathbf{l} \times \mathbf{r}_0\right)}{4\pi r^2} \tag{2.6}$$

and the resulting magnetic flux density in one selected point is [6]:

$$\mathbf{B} = \oint_{C'} d\mathbf{B} \tag{2.7}$$

where μ_0 is the permeability of free space, I current through element, $d\mathbf{l}$ differential loop element, $\mathbf{r}$ displacement vector and r distance from the wire element on a closed path C'. Using this law one could, assuming all constants are known, compute magnetic field from the current. This approach works perfectly on primitive coil geometries, but becomes extremely difficult to solve when more complicated geometries are to be used. General solutions are usually available only when a complex simulation is performed. It appears that other methods have to be used instead of theoretical computations to assess magnetic field shape.

2.1.3 Radiofrequency fields

First we need to explain what is meant by a radio frequency field. In short a RF field is a time-variable electromagnetic field with frequency in the radio frequency range i.e. $3 \text{ kHz} - 300 \text{ GHz}$.

RF coil's magnetic field can be described as a vector sum of individual components of that field. Suppose that separate components are known, then [7]

$$\mathbf{B} = B_x \hat{\mathbf{x}} + B_y \hat{\mathbf{y}} + B_z \hat{\mathbf{z}} \tag{2.8}$$

where $(\hat{\mathbf{x}}, \hat{\mathbf{y}}, \hat{\mathbf{z}})$ form the standard basis in $\Re^3$; the magnitude of the magnetic field $\mathbf{B}$ can be obtained from equation (2.6). The resulting formula is then

$$\| \mathbf{B} \| = \sqrt{|B_x|^2 + |B_y|^2 + |B_z|^2} \tag{2.9}$$

Considering equations (2.8) and (2.9) the magnetic field magnitude can be acquired by successively orienting the probe in the corresponding plane directions, thus measuring the relevant field component. The above mentioned formulas however apply only when magnitude of the signal alone is considered. One cannot simply add phase components to obtain a single value. The phase measured gives information about the direction of the magnetic field vector. A single measurement can thus be written as a complex number in the exponential form

$$\mathbf{B}_k = |\mathbf{B}_k| \, e^{i\phi} \tag{2.10}$$

$$\mathbf{B}_k = |\mathbf{B}_k| \, (\cos{(\phi)} + j \sin{(\phi)}) \tag{2.11}$$

or in the polar (equation 2.11) form, where $|\mathbf{B}_k|$ is the magnitude and ϕ is the phase of the signal. The principle explained here is used in section 3.4 on the measured data.

2.1.4   Principle of reciprocity

As already mentioned, the *Principle of reciprocity* is one of the major laws applied during MRI/MRS examinations. The applicability of the principle on magnetic resonance signals was proven a long time ago by Hoult and Richards [8]. The derivation is, however, difficult and requires good understanding of electromagnetic field theory and magnetic resonance principles, while an experimental proof is quite straightforward to perform [1]. The idea behind the experiment is that when two coils are connected to a network analyzer, the transfer function of the signal between them should not differ depending on which of the coils is used as a receive or transmit coil.

Exactly as explained in section 2.1.1, if a current $I_0 \cos(\omega t + \phi)$ is applied to a transmit coil then, based on eq. (2.3), a magnetic moment $m = I_0 A \cos(\omega t + \phi)$ is created perpendicular to the plane of the coil. The distribution of this field is very difficult to assess (especially for higher frequencies), however, when the component perpendicular to the plane of the receiver loop passes through it a voltage $V_p = -Ad\mathbf{B}_p/dt$ is induced. This voltage is recorded by the network analyzer and displayed as a function of frequency. The equation above is a direct application of Faraday's law and can be used because the coils are designed to be responsive only to the magnetic component of the electromagnetic field. For detailed derivation of the principle in the area of MR the reader is advised to consult literature [1, 8].

2.2   Magnetic resonance phenomenon

Although describing the phenomenon of magnetic resonance is not the focus of this work, we believe that a short introduction to the area needs to be given in order for the reader to appreciate our efforts. For a throughout review of the topic many excellent books exist such as [9, 10].

2.2.1   Nuclear spin

Some atomic nuclei, for example ^{1}H or ^{31}P, posses a property called spin which is usually visualized as a spinning motion of the nucleus along its axis [11]. With the spin a magnetic property comes, so that when the spins are placed in a static magnetic field $\mathbf{B}_0$ they will align along the field. The frequency of the precession is called Larmor frequency and is dependent on the strength of the external field. The frequency is expressed by

$$\omega = -\gamma \mathbf{B}_0 \qquad (2.12)$$

where γ is the gyromagnetic ratio, which is different for every nuclear isotope, and $\mathbf{B}_0$ is the magnitude of the static magnetic field. We should mention for example ^{1}H at $\mathbf{B}_0 = 1.5$ T has $\omega = 63.9$ MHz, for ^{31}P is $\omega = 25.85$ MHz.

The spins can align in two directions, which slightly differ in energy, as can be seen in figure 2.1. One can force the spins to change their energy level by applying an RF pulse (called the $\mathbf{B}_1$ field) perpendicular to the $\mathbf{B}_0$ field plane,

while fulfilling requirement given by

$$\Delta E = 2h\pi\omega_0 \qquad (2.13)$$

where ΔE is the energy difference between the levels and h is the Planck constant ($h = 6.626\ 068\ 96 \times 10^{-34}$)
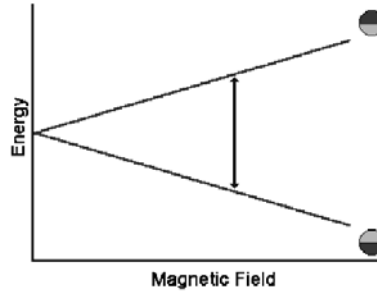

Figure 2.1: Energies of the two orientations of nuclear spin, taken from [12]

2.2.2 ^{31}P NMR spectroscopy

When an layman is exposed to NMR in health care, it is usually in the form of MRI — Magnetic Resonance Imaging. But another examination modality also exists; it is known as MRS — Magnetic Resonance Spectroscopy. The difference between the two methods is that while MRI gives visual and structural information, MRS reveals information on composition of the object examined.

Every time a static field $\mathbf{B}_0$ is applied on a nucleus, a new small local magnetic field appears with the magnitude dependending on strength of the main $\mathbf{B}_0$ field. As a result, the total field at the nucleus can be written as [11, 9]

$$\mathbf{B}_{eff} = \mathbf{B}_0(1 - \sigma) \qquad (2.14)$$

where σ is the contribution of the electrons. Using eq. (2.12) we get to

$$\omega_0 = -\gamma\mathbf{B}_0(1 - \sigma) \qquad (2.15)$$

which is the resonance frequency for a specific nucleus.

A difference of resonance frequencies from an arbitrarily chosen frequency is known as chemical shift and is usually expressed in dimensionless units - part per million (ppm) [11]. The variations are due to the fact that in different compounds different bindings are used and therefore $\mathbf{B}_{eff}$ values will slightly differ. A sample ^{31}P spectra of human liver is displayed in figure 2.2. Each resonance peak represent a different chemical compound, such as α-ATP, β-ATP, γ-ATP, etc. Based on this information, one can reveal the composition of the tissue.
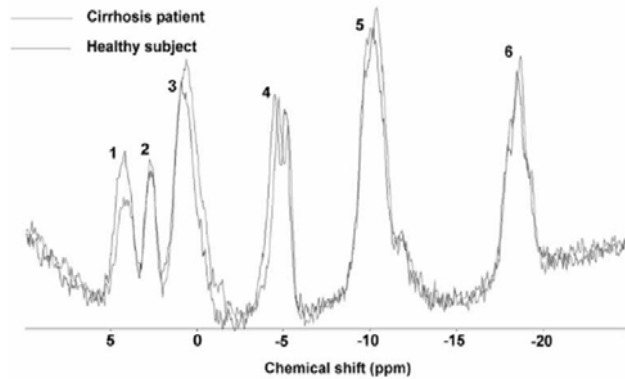
Figure 2.2: Human liver ^{31}P MRS spectrum; 1–PME, 2–Pi, 3–PDE, 4,5,6–ATP

2.2.3   Absolute quantification

As explained in previous section, magnetic resonance spectroscopy gives information about the composition of an object. Unfortunately, the way to obtain quantitative information is not straightforward. For absolute quantification of the signals the measured spectrum needs to be compared to a spectrum of a reference substance with known concentration [13]. Moreover, compensations for changes of the sensitivity caused by variable load and $\mathbf{B}_1$ field inhomogeneities must be performed [14].

In conclusion, in order to obtain absolutely quantified MRS signals knowledge about the RF coil's $\mathbf{B}_1$ field is essential.

Chapter 3

Materials and methods

This chapter describes used equipment, implemented algorithms, and fully explains the process of obtaining results.

3.1 Hardware setup

The proposed method to acquire EM field maps utilizes an industrial coordinate table (Solectro AB, Lomma, Sweden), a vector network analyzer (R&S ZVB4, Rohde&Schwarz GmbH, Munich, Germany), and a personal computer. The setup also involves a voltage-level converter which transforms coordinate table's 24 V output voltage to a TTL level compatible with used A/D card (NI USB-6008, National Instruments Corp., Austin, Texas, USA). The connection diagram of the whole setup is displayed in figure 3.1. The coordinate table is controlled using the J-Cam® software (Solectro AB, Lomma, Sweden) and all data are processed using the MATLAB® R14 (The MathWorks Inc., Natick, Massachusetts, USA) computing environment. Separate components of the measurement chain will be described in detail in following sections.

3.1.1 Coordinate table

The coordinate table is a three-axis robot being capable of autonomous movements. It is used to move H-field (also known as near field) probes over the scanned area with high accuracy (max. resolution 0.25 mm). From its design (see figure 3.2b) it is clear that it is well suited for the proposed method; the metal parts of the robot body are far enough from the sample not to introduce distortions into measurements, moreover the base plate of the table is made of PVC covered flake board to avoid coupling to the coils.

The table is equipped with an industrial PLC unit and its movement is controlled by G-code routines. G-code is a name for programming code originally developed to control CNC (CNC stands for computer numerical control) machines. In our case the usual difficulty of G-code programming is reduced to a rather sim-
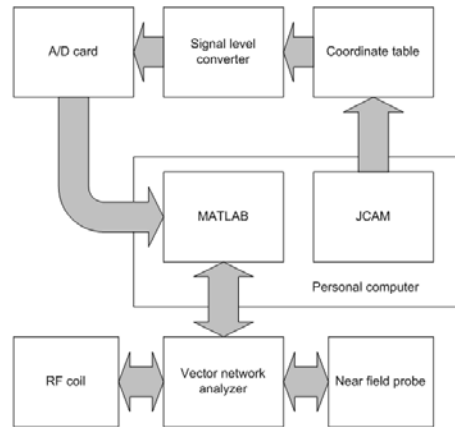
Figure 3.1: Hardware connection diagram

ple routine, because the coordinate table supports only a limited number of CNC commands.

Since the robot is not equipped with any feedback sensors it cannot detect hitting an obstacle; this must be taken into account when designing steering routines. The result of a collision could result in destroying the sensing probe or capsizing the tank with saline solution (see figure 3.2b).
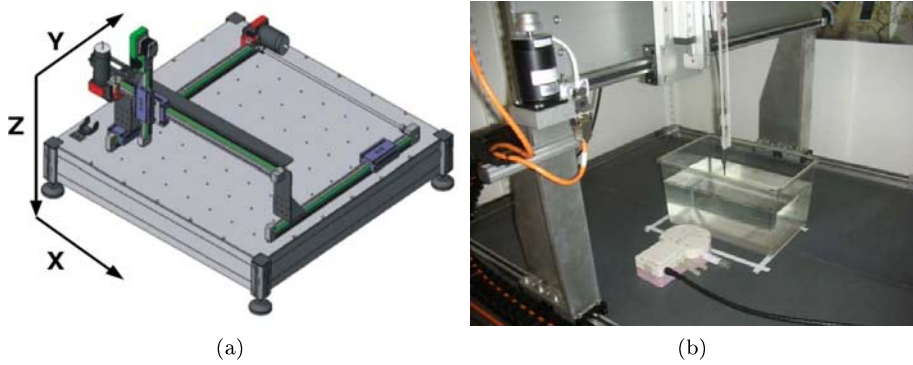

(a)   (b)

Figure 3.2: Coordinate table (a) axis convention (b) RF coil, water tank and a near field probe. Schematics adjusted from [15].

The axes are denoted as in figure 3.2a and since they are not corresponding to axes usually used in MR examinations a coordinate transformation is needed. More details about axes and coordinate system transformations will be presented further on in this chapter.

All CNC programs are written in the J-Cam $^{®}$ environment and sent to the robot over serial link to perform demanded operations. The programs can be ex-

ecuted both directly from PC or copied to the internal memory of the PLC and run from there. The second solution proved itself to be more reliable due to MS Windows$^{\text{TM}}$process handling, which hampered seamless coordinate table control.

The coordinate table's PLC offers serial port connectivity and standard PLC 24 V level inputs and outputs. However, because there are no drivers for MATLAB® software for the machine, controlling had to be done by the abovementioned J - Cam ® software. Initially, we had to focus on concurrence with other laboratory equipment during the measurements; one of the first tasks was to implement reliable timing mechanisms. As can be seen in figure 3.6, the PLC is triggering the A/D card, which then requests new sweep from the analyzer. This sweep is then saved into a file by a MATLAB® callback function. Since the PLC is originally meant for industrial use it only supports standard two-level 0/24 V output. To accommodate this voltage range for the A/D card trigger input, a conversion circuit to TTL levels had to be designed and created. Its circuit diagram is shown in figure 3.3.
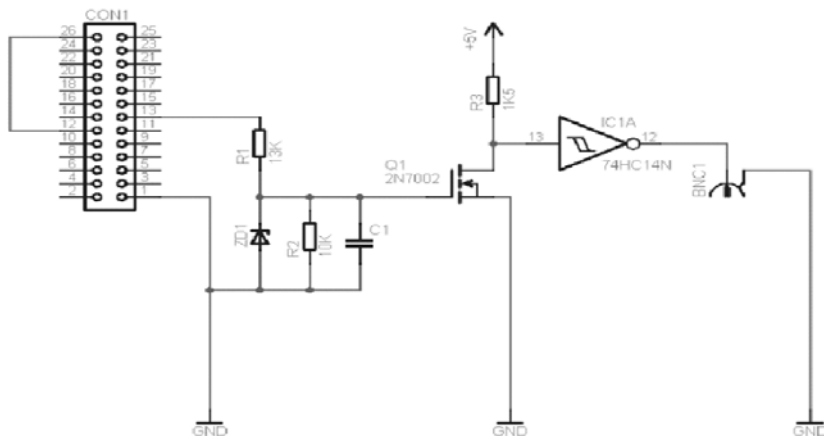
Figure 3.3: Voltage level converter

As could be seen, the converter's circuit is a relatively uncomplicated one. It uses a single Zener diode to limit voltage of the input. An N-channel MOS transistor (2N7002) in conjunction with a pull-up resistor on drain is used to obtain accurate TTL level output signal. However, since small overshoots were discovered after throughout inspection of the output signal, an inverting Schmitt trigger circuit (74HC14N) was added to produce accurate TTL signal on the circuit output.

Because the designed test setup is expected to be used in future research, a function in MATLAB® which creates a G-code routine was written. Like this, operator does not need to learn CNC programming language and instead enter few parameters in a MATLAB® function with which he/she is probably already familiar with. This also works as a safety mechanism, safety checks are implemented

in the function.

3.1.2   Vector network analyzer

The instrument provides information about properties of electrical networks, such as reflection and transmission — referred to as scattering (or S-) parameters — usually at high frequencies [16, 6]. Compared to a regular network analyzer, a vector network analyzer has the ability to measure both magnitude and the phase of the signal, while network analyzer lacks the capability of phase measurements. More information about the S-parameters can be found in appendix A.

  According to the theory, the forward and reverse parameters S_{12} and S_{21} should be equal. There are, however, always differences in values because of for example surrounding electromagnetic (EM) noise. Nevertheless, we assume that these variations could be neglected in our application. Due to the setup of our experiment, where a +20 dB amplifier is used, one sweep for which both magnitude and phase is stored is performed for every particular point of the RF coil.

  The analyzer is configured and triggered over the GPIB bus using MATLAB$^{\circledR}$ and Instrument Control Toolbox$^{\text{TM}}$; data are stored using functions available in the Data Acquisition Toolbox$^{\text{TM}}$. The flowchart of the whole process is displayed in figure 3.6.

3.1.3   A/D card

Several different possibilities of synchronizing the equipment were assessed, but the solution using an A/D card was chosen as the most reliable one. The reason for difficulties with synchronization is J-Cam$^{\circledR}$'s inability to communicate directly with the MATLAB$^{\circledR}$ environment; because of this we needed to come up with a workaround. National instruments NI-6008USB A/D card is used in this work, it is a relatively cheap solution, yet fully sufficient for our needs. Drivers for MS Windows$^{\text{TM}}$and MATLAB$^{\circledR}$ are available from the manufacturer. The digital trigger input, which was used on the card, requires TTL leveled inputs. As already mentioned, to overcome this, a converter board was designed. To summarize: The A/D card is used in order to give MATLAB$^{\circledR}$ a mean of synchronization between the network analyzer and the coordinate table.

3.1.4   H-field probes

An H-field probe is a special coil which does not respond to the electrical component of the EM field and thus measures only the magnetic (or H-) component of it. In the early stages of the project the measurements were performed using an in-house made pickup coil. Due to limited resolution and positioning difficulties, commercially available H-field probes (LANGER EMV-technik GmbH, Bannewitz, Germany) were chosen instead. Two different probes are used; one to measure in planes parallel to the RF coil (figure 3.4) and one to pickup magnetic flux emanating perpendicular to the RF coil plane (figure 3.5). Scans were

acquired sequentially for each component of the magnetic field; probes were manually rotated or exchanged between separate scans. The positioning is shown in figures 3.4a and 3.5a.
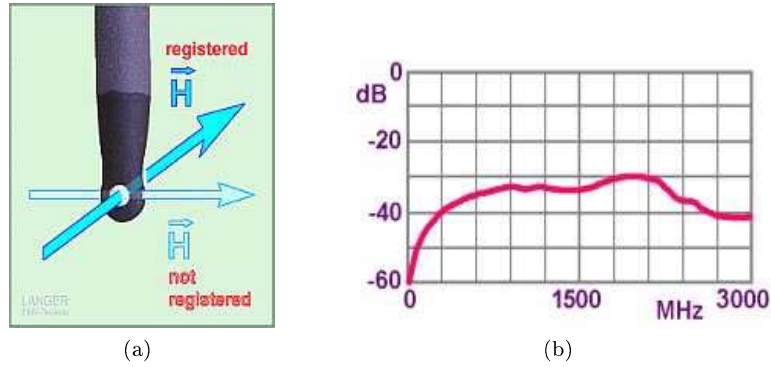

(a) (b)

Figure 3.4: Search coil RF–1 and its transfer function, taken from [17]
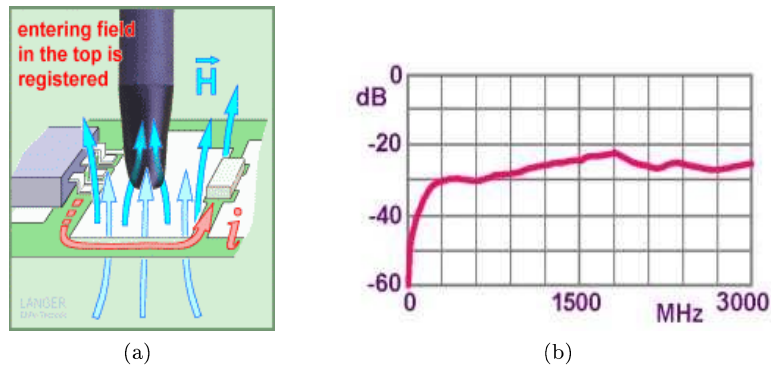

(a) (b)

Figure 3.5: Search coil RF–3 and its transfer function, taken from [17]

3.2   Data acquisition

MATLAB® controls almost the whole measurement process in our setup. In figure 3.6, one can observe how the process works. First, the coordinate table sends a trigger signal and this signal is then sensed by the A/D card. Since the A/D card trigger event is handled by a MATLAB® callback function, the software environment can send a sweep request via GPIB bus to the vector network analyzer and read current measured data. Data are saved immediately in a file on the computer's hard drive, because the amount of information obtained during detailed measurements is large enough to overload RAM. A special initialization function was written to ease initial setup of the analyzer and the A/D card.
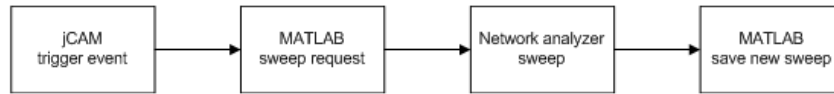
Figure 3.6: Event flowchart

3.2.1 Scanning preparation tasks

A Philips ^{31}P MRS RF coil was used for the experiments. Although the principles identified later hold generally, they will be for the sake of simplicity explained using this coil. As described in chapter 2.2, Larmor frequency varies slightly throughout the scanned subject due to applied gradient fields of the scanner. This enables spatial coding of the data, but could introduce variations when excitation of the spins should take place. This effect is neglectible compared to variations caused by human body loading. Both inductance and capacitance changes detunes the coil, hence to guarantee correct and constant flip angles in the whole excited volume, coil tuning and matching must be performed before every measurement. For the Philips MRS coil both tuning and matching is done manually by changing values of built-in variable capacitors.

In the measurement protocol both tuning and matching were performed before each measurement with the help of the network analyzer and the output reflection coefficient S_{22}. In short, the circuit is matched when there is no reflection — this can easily be seen as a significant drop in the transfer function; on the other hand, tuning moves the magnitude drop in frequency until the desired frequency is reached. From this the process of coil tuning and matching is obvious: One tries to find maximal dip at a specified frequency. Figure 3.7 shows a plot of a transfer function after tuning and matching was performed.

The next step run before the scanning is initialization of the network analyzer. In order to significantly simplify the procedure an initialization function in MATLAB$^{\circledR}$ is used. This clears analyzer's memory, sets demanded parameters and configures measurement behavior.

3.2.2 RF coil scanning

RF coil's EM field scanning is a tedious task. There are many reasons that together create a time consuming measurement. Robot arm movement, time necessary to let the search coil settle down to avoid vibrations, network analyzer finite sweep time, analyzer to PC data transfer; they all typically take time much shorter than a second. However, since a regular scan involves around 16 000 repetitions of the process displayed in figure 3.6 one could imagine the demands on time and repeatibility. In order to minimize scan time special trajectory of the probe was proposed. The scanning pattern for one layer of the scan can be seen in figure 3.8. After completing one plane the probe is raised, returned to the starting position (depicted by a dot in figure 3.8) and the whole process is repeated.

A drawback of this method is the necessity of scan data post-processing; the data matrix has to be reshaped and unfolded to obtain dataset corresponding to
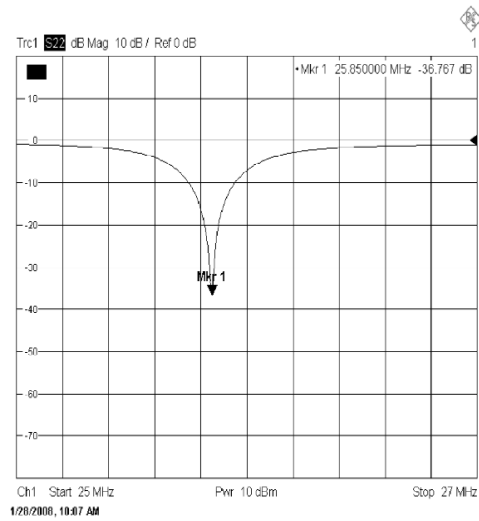
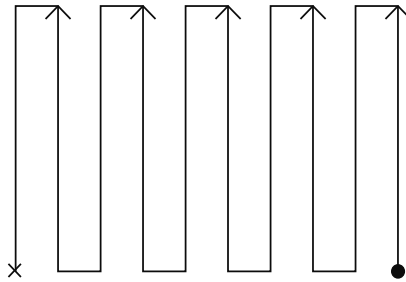Figure 3.7: Correctly tuned and matched coil transfer function

Figure 3.8: One layer scanning pattern

real world geometry. One could also easily notice that extra measurements are introduced, but their impact on final scan time is neglectible.

Data reformatting is required in order to sort the data in a more logical way and it consists of following steps:

- removal of extra points (denoted by a cross in figure 3.8)

- reshaping of the dataset from a single vector to a matrix

- flipping each odd line

3.2.3   Frequency sweep

To enable review of previously acquired data and to maximize the information obtained from each measurement a frequency sweep is performed for every distinct position above the RF coil. The parameters used are $f \in \langle 25, 27 \rangle$ MHz with a frequency bandwidth of 10 kHz. In this interval 201 points are obtained.
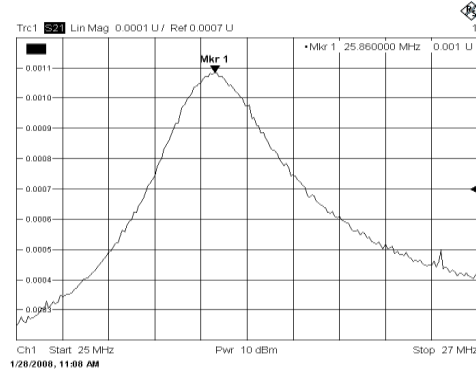
Figure 3.9: Single sweep

Since for ^{31}P spectroscopy at $\mathbf{B}_0$=1.5 T we are interested primarily in frequency f=25.85 MHz, which is the Larmor frequency of phosphorus, a single corresponding point is chosen from the sweep data vector. This process is repeated for every distinct point on the coil until new dataset consisting only of magnitude (and/or phase) values at a specified frequency is created. A plot of a single sweep is displayed in figure 3.9, the point which corresponds to Larmor frequency is marked. An example of how the points at which the scanning is performed can be selected is shown in figure 3.10.
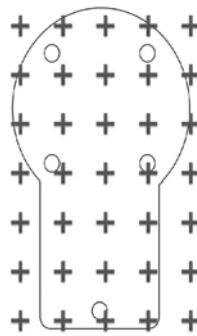
Figure 3.10: Example of scan point selection

3.3 MR data processing

In this section all MR data processing steps will be described in detail, some steps which are less relevant are throughougly explained in the appendixes.

Imaging data on the Philips Achieva 1.5 T MR scanner systems are saved in Philips proprietary .par and .rec files. Raw data are byte-to-byte stored in the .rec file while the .par file contains meta-information, such as voxel orientation, number of points, number of slices, voxel size and much more. An in-house developed reading function was used to convert data from the .rec file using the .par file into MATLAB® workspace.

Spectrum data are stored in .spar and .sdat files on the Philips MR systems. Similarly to image files a .spar file contains information about the spectrum voxel (such as orientation, size...) and an .sdat files contain raw data.

3.3.1 Coordinate system transformations

As one can imagine from the discussion above it is possible, by using information stored in the .par file, construct a conversion matrix $\mathbf{M}_{im}$, which describes the coordinate transformation from the scanner isocentre to image voxel centre. (An isocentre is the origo of MR scanner's coordinate system and it is also the point where the $\mathbf{B}_0$ field is most homogeneous.) Likewise, a conversion matrix $\mathbf{M}_{sp}$ can be constructed to describe transformation from scanner isocentre to spectrum voxel center. Knowing both matrixes a transformation matrix from spectrum to image voxel coordinate system can be created. An throughout description of .par and .spar files can be found in appendix B.

Transformation matrix concatenation

In general, a transformation matrix $\mathbf{M}$ can be written as

$$
\begin{aligned}
\mathbf{M} &= \left[\begin{array}{cccc} & \mathbf{R} & & \mathbf{T} \\ 0 & 0 & 0 & 1 \end{array} \right] \\
&= \left[\begin{array}{cccc} R_{1,1} & R_{1,2} & R_{1,3} & x \\ R_{2,1} & R_{2,2} & R_{2,3} & y \\ R_{3,1} & R_{3,2} & R_{3,3} & z \\ 0 & 0 & 0 & 1 \end{array} \right]
\end{aligned}
\tag{3.1}
$$

where $\mathbf{R}$ is the rotation matrix and $\mathbf{T}$ the translation matrix. Using the $\mathbf{M}$ matrix transformation in space can be performed. How exactly the rotations are performed is explained in following sections.

Euler angles

Rotating a coordinate system is in principle similar to rigid body rotations. Such a rotation can be performed provided one knows three exact parameters – one set

of these can be the Euler angles. A matrix (in the homogenous form) describing rotation around an axis has following structure

$$
\mathbf{R}_x(\varphi) = \begin{bmatrix} 1 & 0 & 0 & 0 \\ 0 & \cos(\varphi) & \sin(\varphi) & 0 \\ 0 & -\sin(\varphi) & \cos(\varphi) & 0 \\ 0 & 0 & 0 & 1 \end{bmatrix} \tag{3.2}
$$

$$
\mathbf{R}_y(\varphi) = \begin{bmatrix} 1 & \cos(\varphi) & -\sin(\varphi) & 0 \\ 0 & 1 & 0 & 0 \\ 0 & \sin(\varphi) & \cos(\varphi) & 0 \\ 0 & 0 & 0 & 1 \end{bmatrix} \tag{3.3}
$$

$$
\mathbf{R}_z(\varphi) = \begin{bmatrix} \cos(\varphi) & \sin(\varphi) & 0 & 0 \\ -\sin(\varphi) & \cos(\varphi) & 0 & 0 \\ 0 & 0 & 1 & 0 \\ 0 & 0 & 0 & 1 \end{bmatrix} \tag{3.4}
$$

3.3.2   Rotation order

There is a specific problem when performing rotations using the Euler angles and that is there is no standard convention for rotation order. By using trial and error it was found that the correct multiplication order for imaging voxel on Philips Achieva systems stored in .par file is **ZYX** (valid for all system versions).

For the spectrum voxel (saved in the .spar file) the multiplication order was found to be **ZXY** (system version 2.1.3), this however changed after upgrading the MR system and the current order is **ZYX** (system version 2.5.1 and newer) — unexpectedly the same as in the imaging voxel. More details on this topic can be found in appendix C

3.3.3   Transformations of MR coordinate systemts

We have shown the Euler angle rotation order and defined the coordinate systems. Now the transformation matrixes can be introduced. The transformation matrix from the scanner coordinate system to the imaging coordinate system is given by equation

$$
\mathbf{X}_{im} = \mathbf{R}_z\mathbf{R}_y\mathbf{R}_x\mathbf{T}\mathbf{X}_{sc} = \mathbf{M}_{im}\mathbf{X}_{sc} \tag{3.5}
$$

where $\mathbf{X}_{im}$ are coordinates in image coordinate system and $\mathbf{X}_{sc}$ in the scanner system. The transformation from scanner coordinate to spectrum coordinate system is described by equation

$$
\mathbf{X}_{sp} = \mathbf{R}_z\mathbf{R}_y\mathbf{R}_x\mathbf{T}\mathbf{X}_{im} = \mathbf{M}_{sp}\mathbf{X}_{im} \tag{3.6}
$$

where $\mathbf{X}_{sp}$ are coordinates in spectral system. Using both equations (3.5) and (3.6) the conversion between spectral and imaging coordinate system is given by

$$
\mathbf{X}_{im} = \mathbf{M}_{im}\mathbf{M}_{sp}^{-1}\mathbf{X}_{sp} \tag{3.7}
$$

$$\mathbf{X}_{sp} = \mathbf{M}_{sp}\mathbf{M}_{im}^{-1}\mathbf{X}_{im} \tag{3.8}$$

Since we now have the matrix of points to be transformed we can, using equation (3.7), perform transformations from spectrum to scanner coordinate system, and with help of equation (3.8) transform coordinates from image to spectrum coordinate system.

3.3.4 Image and spectroscopy data intersection

In order to display and recreate the position of the spectrum volume of interest (VOI) in the image data a line-plane intersection function is implemented as a MATLAB$^{\circledR}$ function.

Each plane is determined by three points x_1, x_2, and x_3. A line passing through a plane can be described by two points x_4 and x_5. Then the line intersects the plane in a point which can be determined by solving a linear equation system [18]

$$\mathbf{0} = \begin{bmatrix} x & y & z & 1 \\ x_1 & y_1 & z_1 & 1 \\ x_2 & y_2 & z_2 & 1 \\ x_3 & y_3 & z_3 & 1 \end{bmatrix} \tag{3.9}$$

$$x = x_4 + (x_5 - x_4)\, t \tag{3.10}$$

$$y = y_4 + (y_5 - y_4)\, t \tag{3.11}$$

$$z = z_4 + (z_5 - z_4)\, t \tag{3.12}$$

which for x, y, z and t gives [18]

$$t = -\frac{\begin{bmatrix} 1 & 1 & 1 & 1 \\ x_1 & x_2 & x_3 & x_4 \\ y_1 & y_2 & y_3 & y_4 \\ z_1 & z_2 & z_3 & z_4 \end{bmatrix}}{\begin{bmatrix} 1 & 1 & 1 & 0 \\ x_1 & x_2 & x_3 & x_5 - x_4 \\ y_1 & y_2 & y_3 & y_5 - y_4 \\ z_1 & z_2 & z_3 & z_5 - z_4 \end{bmatrix}} \tag{3.13}$$

when the value $t \geq 0$ and $t \leq 1$ it can be put back into equations (3.10), (3.11) and (3.12) the point of intersection (x, y, z) is obtained [18].

In our case, the points were defined in a following way (described for intersections with transversal plane; the same principle applies for anterior-posterior and left-right planes)

$$\begin{aligned} x_{1k} &= x_1 + (k - 1)\, Z_{size} \\ x_{2k} &= x_2 + (k - 1)\, Z_{size} \\ x_{3k} &= x_3 + (k - 1)\, Z_{size} \end{aligned} \tag{3.14}$$
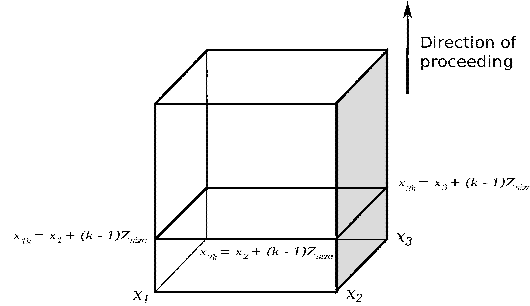
Figure 3.11: Defining planes in imaging voxel

where Z_{size} is the number of slices in the image voxel, the equation is also illustrated in figure 3.11.

Because a cube (voxel) is formed by twelve edges it is necessary to find intersections for all of them. Thus, points x_4 and x_5 are tried according to following scheme

$$x_4 = \{1, 1, 1, 2, 2, 3, 3, 4, 5, 5, 6, 7\}$$
$$x_5 = \{2, 4, 5, 3, 6, 4, 7, 8, 6, 8, 7, 8\} \tag{3.15}$$

where numbers are consecutively numbered vertices (see figure B.1). By looping through the volumes the corresponding intersection points are found and stored.

After the coordinates are found, their values are recalculated to matching indexes in the image volume. This is done by a simple transformation involving translation and scaling (eq. 3.16)

$$\mathbf{X}_{ind} = \mathbf{M}_{conv}\mathbf{X}_{real} \tag{3.16}$$

where

$$\mathbf{M}_{conv} = \begin{bmatrix} X_{size} & 0 & 0 & \frac{-X_{voxel\_size} - X_{size}}{2} \\ 0 & Y_{size} & 0 & \frac{-Y_{voxel\_size} - Y_{size}}{2} \\ 0 & 0 & Y_{size} & \frac{-Z_{voxel\_size} - Z_{size}}{2} \\ 0 & 0 & 0 & 1 \end{bmatrix} \tag{3.17}$$

Using the equation above, the points of intersection could easily be found and displayed. An example is shown in figure 3.12, where the intersection of the spectral voxel with a particular transversal image slice is drawn as a convex shape around five found intersecting points.

3.3.5 MR visible markers

In order to correctly use the measured $\mathbf{B}_1$ field map in the data obtained from the MR scanner, accurate information about the position of the RF coil is required. From the MR data one can extract exact positions and orientations of both spectroscopic and imaging voxels. These however tell nothing about the RF coil's location. To overcome this difficulty we have attached MR-visible markers
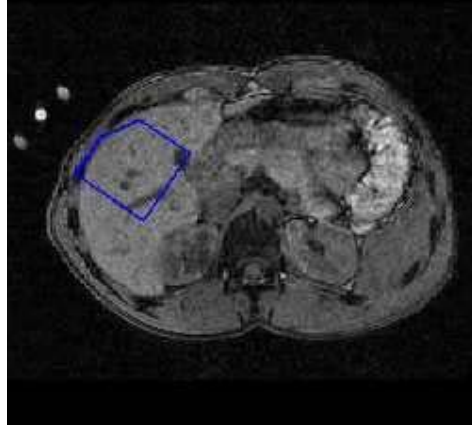
Figure 3.12: Transversal MR image with spectral voxel superimposed. Coil markers can be seen on the upper-left side

to the coil and detected their positions in the image voxel. The markers itself are ordinary vitamine E capsules; these contain oils which are MR visible and more importantly they are not toxic.

Marker localization

A MATLAB$^{\circledR}$ function was written for marker localization. It is based on the assumption that the marker center is in its center of mass. Under this condition already existing MATLAB$^{\circledR}$ functions can be accustomed and then used to find it. The coordinates are found in the image coordinate system. For use in other functions it is neccessary to perform a transformation of the coordinates (coordinate transformations are throughoutly described in section 3.3.1). An example of marker localization function output can be seen in figure 3.13.

Fitting markers to image data

We obtained the MR-visible marker positions in the image system. To be able to produce images in the plane of the coil we need to find a transformation matrix between the RF coil's system and the image system. A simple trick allowed us to solve this problem. By using a least square fitting we were able to find the optimal transformation matrix.

Assume two corresponding datasets $\{m_i\}$ and $\{d_i\}$, where m_i are marker coordinates in image coordinate system, d_i in RF coil's system and $i \in \{1, 5\}$. Then these two sets are related by [19, 20]

$$d_i = \mathbf{R}m_i + \mathbf{T} + \mathbf{V}_i \tag{3.18}$$

where $\mathbf{R}$ is a standard 3x3 rotation matrix, $\mathbf{T}$ is a translation matrix and $\mathbf{V}_i$ is a noise vector. We can assume that there is no noise and find the optimal solution
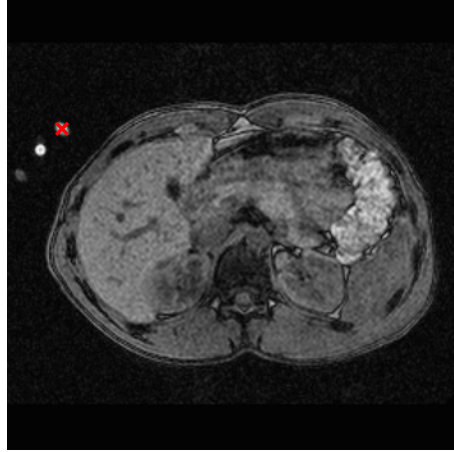
Figure 3.13: MR-visible marker localization. Localized marker is displayed as a red cross in the image.

$[\hat{\mathbf{R}},\hat{\mathbf{T}}]$ by minimizing a least squares error criterion given by [19]

$$\Sigma^2 = \sum_{i=1}^{N} \|d_i - \hat{\mathbf{R}}m_i - \hat{\mathbf{T}}\|^2 \tag{3.19}$$

When matrixes $\hat{\mathbf{R}},\hat{\mathbf{T}}$ are known they can simply be combined in order (see eq. 3.1) to create one matrix to allow for 3D transformations from the image coordinate system to the coil coordinate system for any point. An image from the RF coil's plane at distance $d = 0$, i.e. the coil surface, is displayed in figure 3.14.

Notice the white bar in the figure. This is an image of an external reference which is often used for absolute quantified MR spectroscopy. It consists of 2.831 M DMMP (dimethyl methylphosphonate) and 1‰Magnevist.

3.4   RF data processing

As shown in section 2.1.3, the total magnetic field can be obtained by summing vector components which were obtained separately.

In the measurements the phase of the signal carries information about the direction of the vector component, while the orientation is obtained (for one point) as the sum of all three magnitude components. The phases that are measured could be either $\pi/2$ or $-\pi/2$. Since real numbers to complex are preffered, we choose to add $\pi/2$ to all phase values. This then results in following equations where $k \in \{x, y, z\}$
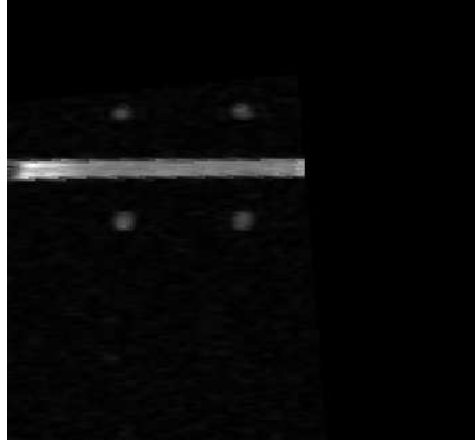
Figure 3.14: Image in the RF coil plane

$$B_k = |B_k|(\cos(\phi) + j\sin(\phi)) = \left\{ \begin{array}{ll} |B_k| & \text{for} \quad \phi = \pi \\ -|B_k| & \text{for} \quad \phi = 0 \end{array} \right. \tag{3.20}$$

A result of the change in phase can be seen in figure 3.15.
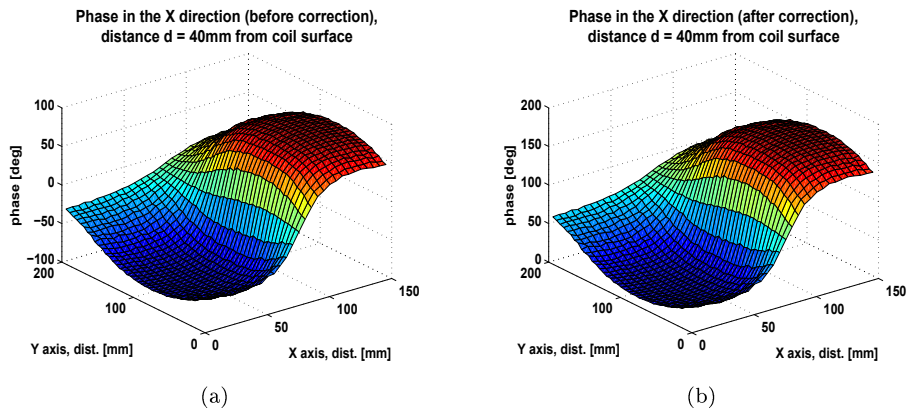
Figure 3.15: Measured phase in the X direction before (a) and (b) after phase correction

Let the coordinate system be defined as in figure 3.16, then when a vector has phase $\phi = \pi$ we say it has positive orientation, i.e. it is in direction of the axis.

3.4.1 Vector field creation

The vector field could now finally be created. First the phase values are processed and then, depending on the value, a conclusion on a corresponding magnitude
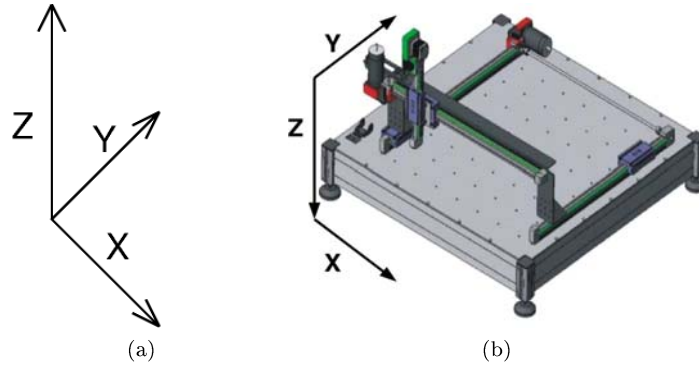
Figure 3.16: Coordinate table (a) axis convention (b) detailed view on the coordinate system. Schematics adjusted from [15].

vector is obtained. At last all three vectors are summed to create a resulting vector for a particular point. An example for one point is shown in figure 3.17, where **r** is the sum of vectors **a**,**b**,**c**. Whole scanned area is looped through to construct a vector field.
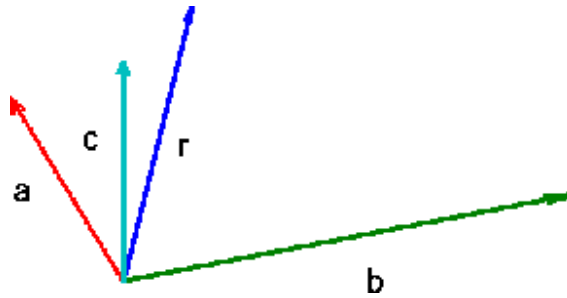
Figure 3.17: Vector sum

B_0 field effect on the RF coil's B_1 field

The $\mathbf{B}_0$ field has a large impact on the RF coil's magnetic field. The most obvious effect is that all components in the plane parallel to the direction of the $\mathbf{B}_0$ do not contribute to measured signal. In the ideal case with the RF coil placed such as the y axis of the RF coordinate system is parallel to $\mathbf{B}_0$ the equation can be changed to

$$\|\mathbf{B}_1\| = \sqrt{|B_x|^2 + |B_z|^2} \tag{3.21}$$

This hardly ever will be the case and because of this we have to find a general projection of the RF coil's field to the scanner system. Based on the definition of the scanner coordinate system from appendix B we know that the z axis of

the scanner coordinate system is in the direction of the $\mathbf{B}_0$ field. Thus, we can utilize a vector from the RF coil's system and transform it into the scanner system and then clear the *z-component* there. After this the vector is transformed back into the RF coil's system. The procedure is easy to understand from following equations; suppose matrix $\mathbf{Z}_{clr}$ is

$$\mathbf{Z}_{clr} = \begin{bmatrix} 1 & 0 & 0 & 0 \\ 0 & 1 & 0 & 0 \\ 0 & 0 & 0 & 0 \\ 0 & 0 & 0 & 1 \end{bmatrix} \tag{3.22}$$

then it can be used in multiplication to clear the z component of any 3D vector. Using knowledge from section 3.3.1 a new equation can be constructed performing projection into $\mathbf{B}_0$ field as

$$\mathbf{X}_{proj} = \mathbf{M}_{co}\mathbf{M}_{im}\mathbf{Z}_{clr}\mathbf{M}_{im}^{-1}\mathbf{M}_{co}^{-1}\mathbf{X}_{rf} \tag{3.23}$$

where $\mathbf{X}_{proj}$ are coordinates of a vector in the RF coil's system including projection, $\mathbf{M}_{co}$ is the transformation matrix from image to coil coordinates and $\mathbf{X}_{rf}$ are the vector coordinates in the RF coil's system.

Chapter 4

Results

This chapter contains all results of the measurements that were performed. The theoretical background as well as the design of the testing procedure was already given in previous chapters of this thesis.

All magnitude plots are normalized to interval $\langle 0, 1 \rangle$. Total $\mathbf{B}_1$ field was reconstructed from raw component data and normalized after summation.

4.1   RF field single component measurements

As explained earlier, a single measurement consists of three separate scans of the RF field. In following figures single planes for every direction are shown. Scans were performed using the near-field probe 50 mm above the RF coil surface. Figure 4.1 depicts magnitude plots.

Figure 4.2 represent phase measurements. Each component is shown in a single image; the plane is in the distance 40 mm from RF coil surface.

4.2   RF field measurements, scalar field

Based on theory (see section 2.1.3, page 7), the separate components can be summed in order to obtain the spatial distribution of the resulting magnetic field magnitude. This can nicely be seen in figure 4.3.

4.3   RF field measurements, vector field

In the theoretical part of this thesis we have explained, that a magnetic field is in fact a vector field. Visualizing a vector field is, compared to a scalar field, much more complicated but since both magnitude and phase were measured, it can be done. Using the phase information one can assign a direction of the vector at a specific point. The output can be seen in figure 4.4. Please note that in order to emphasize the z component, it was plotted in 3D.

(a) X component

(b) Y component

(c) Z component
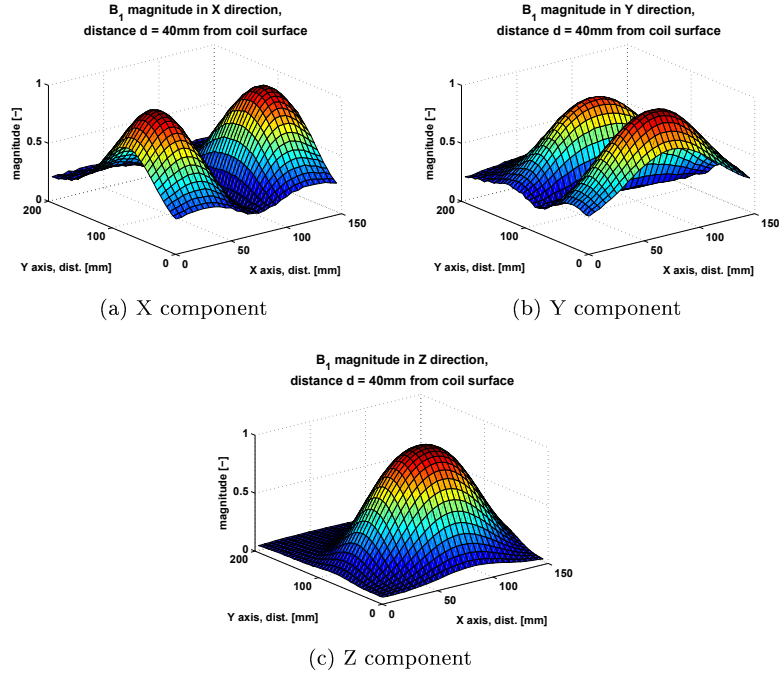
Figure 4.1: Single plane measurement - magnitude.

Using the directional information given by the phases of all the signals, the directions of the fluxlines could be reconstructed. The results can be seen in figure 4.5. When the magnitude plot is combined together with the direction plot one obtains, in our view, a very informative image, which shows both the magnitude of the magnetic field as well as its direction. It is shown in figure 4.6.

4.4 Effect of various media on the measurements

We have tested various media and their impact on the RF coil's magnetic field shape. As expected the properties of media is reflected in the resulting magnetic field shape. We observed that while the magnitude changes only slightly (i.e. it decreases when measured in saline solution), the phase was effected much more. The difference between RF field measured in air and in water can be clearly seen in figure 4.7

4.5 MR data visualization

When working with the MRI/MRS data many transformations are neeeded in order to determine the final result. This section summarizes all those operations. First, the proper transformations had to be found, resulting figures are 4.8 and 4.9.

(a) X component

(b) Y component

(c) Z component
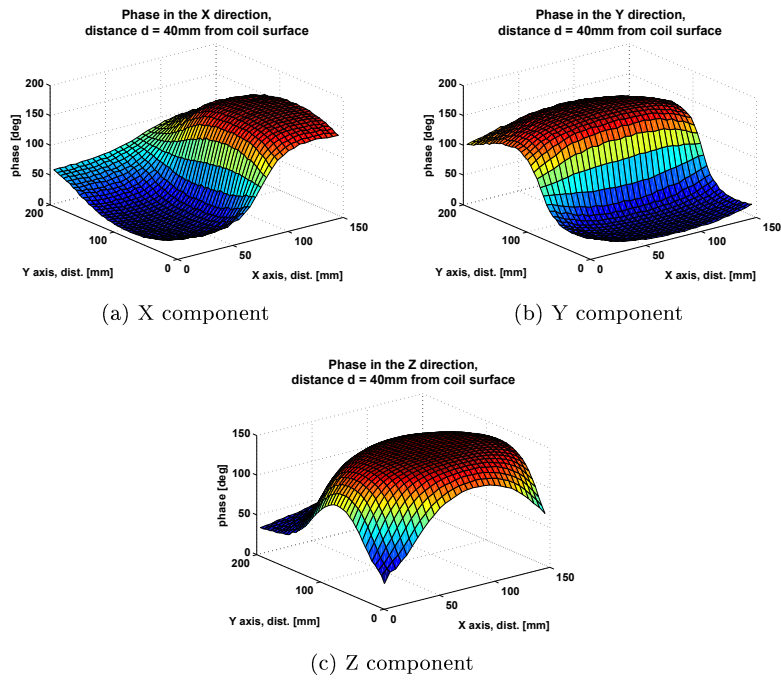
Figure 4.2: Single plane measurement - phase.
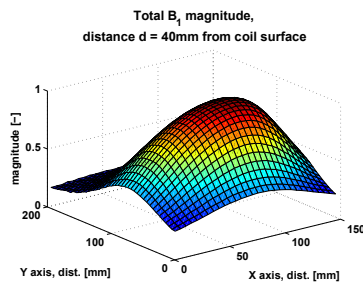
Figure 4.3: Total magnetic field magnitude

In the previous chapter images transformed to coil coordinate system and images with image-spectroscopy voxel intersection were shown. For future work, information about the spectroscopy voxel in the RF coil coordinate system are most important. A sample image is shown in figure 4.10. Since the figure is from the RF coil's reconstructed plane one should keep in mind that the coil is 40 mm 'below the paper'.

Images displaying RF coil's magnetic field, MR image and spectroscopy voxel information follow in figure 4.11.

(a) X component

(b) Y component
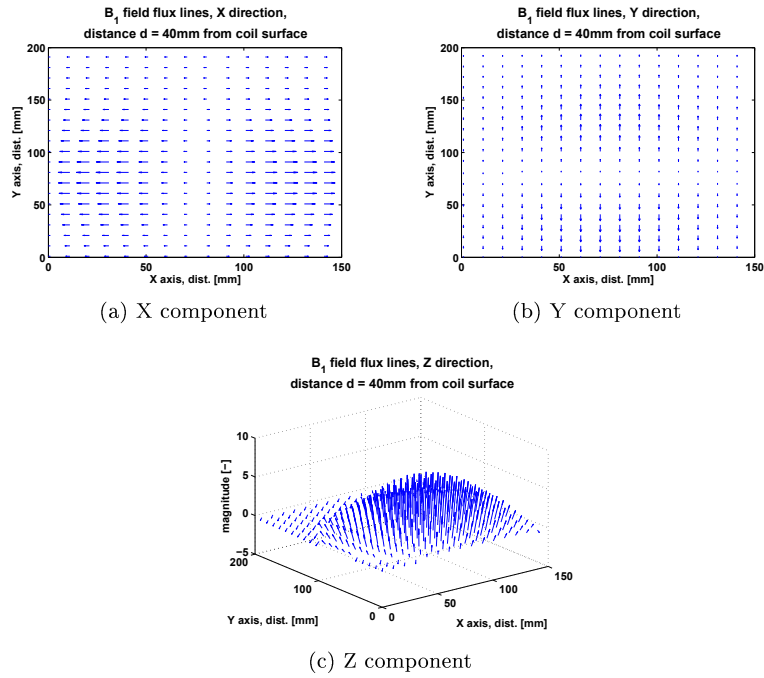
(c) Z component

Figure 4.4: Flux lines
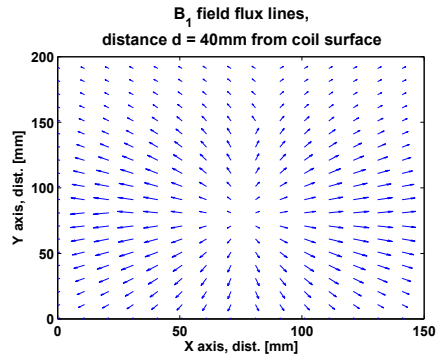
Figure 4.5: Flux lines - Sum of all components

4.6 B_1 field and the MR scanner's main magnetic field

As already described in section 3.4 the RF coil's $\mathbf{B}_1$ field was affected by the MR scanner's main magnetic field $\mathbf{B}_0$. In real measurements it is not possible to obtain signals from the $\mathbf{B}_0$ field direction. Clearly in order to provide correct $\mathbf{B}_1$ field maps one need to perform a correction of the measured data. Using
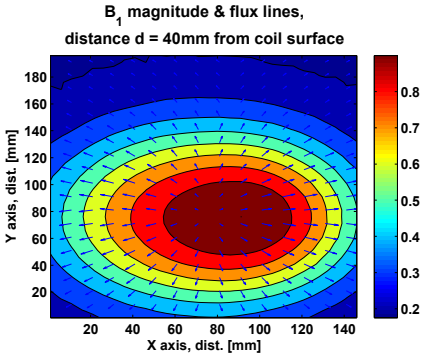
Figure 4.6: Complete map with both magnitude and phase information
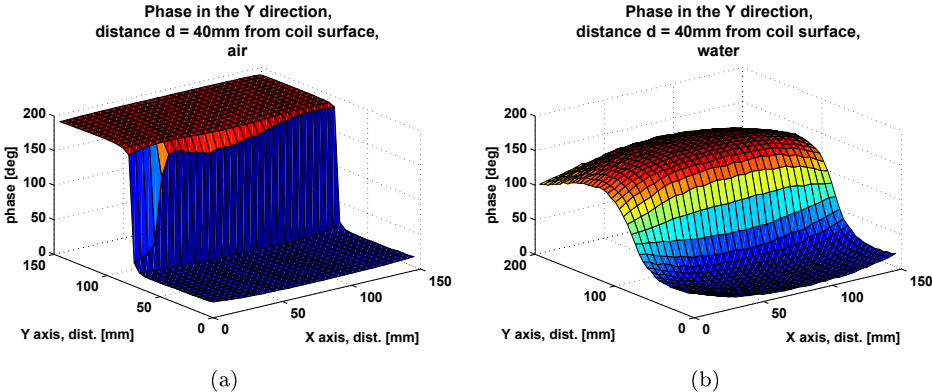
Figure 4.7: The effect of media on the RF field phase. (a) phase in the Y direction in air (b) phase in the Y direction in water.
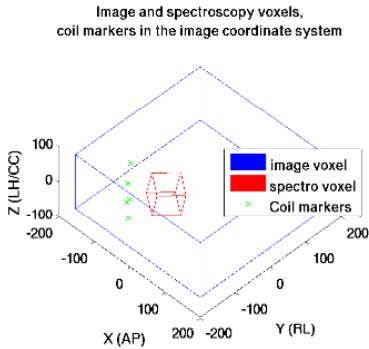
Figure 4.8: Voxels and RF coil markers in image coordinate system
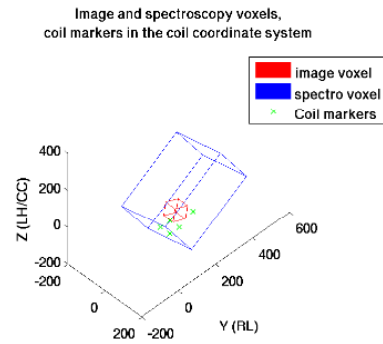
Figure 4.9: Voxels and RF coil markers in coil coordinate system
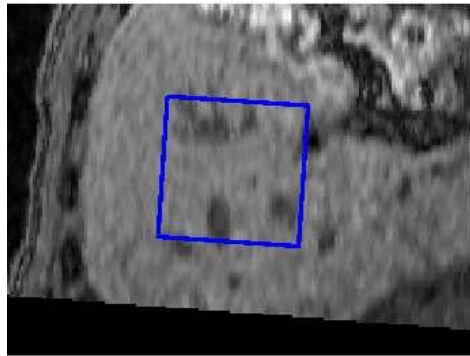
Figure 4.10: Spectroscopy voxel in coil coordinate system, the coil is placed 50 mm 'below the paper'.

equations 3.22 and 3.23 (for RF coil position as in figure 4.9) the effective $\mathbf{B}_1$-field was recalculated. Figure 4.12 shows the flux lines of the $\mathbf{B}_1$-field after projection, and figure 4.13 displays the magnitude of the field after projection. It is readily seen that while the magnitude is not strongly affected, the flux of the signal is heavily distorted.

<div align="center">(a)   (b)</div>
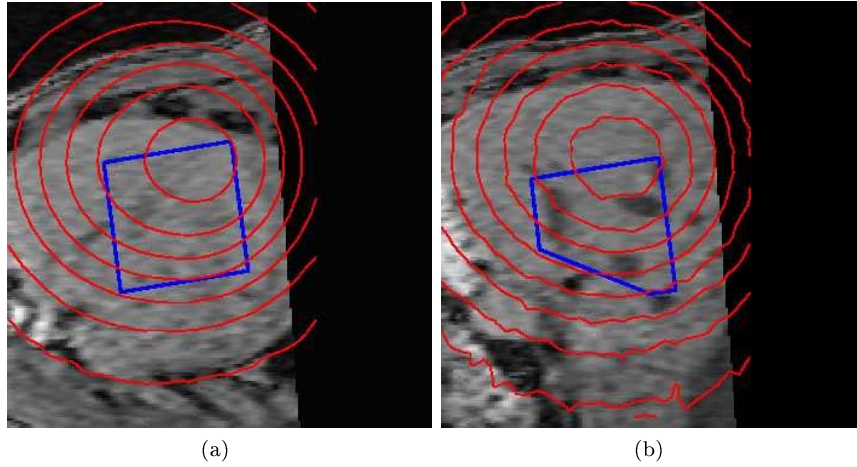
Figure 4.11: Combination of MR image, MR spectroscopy data and RF map. (a) at a distance of 50 mm and (b) at a distance of 80 mm from the RF coil.
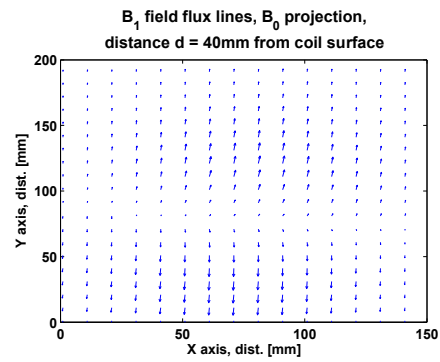
Figure 4.12: Flux lines - sum of all components; after projection
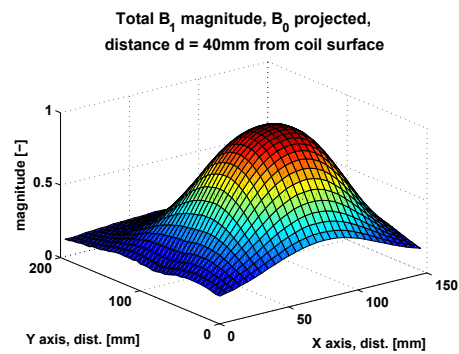
Figure 4.13: Total magnetic field magnitude after projection

Chapter 5

Conclusion

In this master thesis we have implemented a method of direct measurement of the $\mathbf{B}_1$ field outside the MR scanner in order to obtain exact values of flip angles and to serve as a source for correction data in quantitative spectroscopy (MRS).

We are aware of the fact that other $\mathbf{B}_1$ assessment methods exist, such as measurements inside the scanner. These methods, however, do not give any information on the phase of the signal, thus one can not construct a vector field from the information obtained. Another drawback of these methods is that no signal can obtained from the $\mathbf{B}_1$ field direction, so a user never gets a complete picture of how the RF field is spatially distributed. Our proposed method can solve both these problems and, based on relevant theory, we believe it gives an accurate and reliable information about the $\mathbf{B}_1$ field. Complete validation of the method has not been yet performed, we propose to validate the $\mathbf{B}_1$ field's magnitude distribution using an in-scanner method, alternatively using a software package QRAP developed at the department.

Working with the MR data was more complicated than anticipated as many rigid body and coordinate system transformations were required. Validation of these operations, although time-consuming, was performed as shown for example in figures 4.8 or 4.9 .

The results obtained from this thesis work will be used in further research on absolute quantified spectroscopy.

Bibliography

[1] Hoult DI. The Principle of Reciprocity in Signal Strength Calculations - A Mathematical Guide. Concepts in Magnetic resonance. 2000;12:173–187.

[2] Sykora S. Antenna Reciprocity Theorem in Magnetic Resonance - A summary; 2001. `http://www.ebyte.it/library/educards/nmr/Nmr_AntennaTheorem.html`. online.

[3] G H, Evalappan SP, Hirata H. Mapping of the B1 field distribution of a surface coil resonator using EPR imaging. MRM. 2002;48:1057–1062.

[4] Jerschowa A, Bodenhausen G. Mapping the B1 Field Distribution with Nonideal Gradients in a High-Resolution NMR Spectrometer. JMRE. 1999;137:108–115.

[5] Dahlquist O, Cohen L, Lund E, Lundberg P. Absolute quantification of 31P muscle MRS using B1-field mapping. In: ISMRM Thirteenth Scientific Meeting and Exhibition, Miami Beach, Florida, USA; 2005. .

[6] Cheng DK. Field and Wave Electromagnetics. Addison-Wesley Publishing Company Inc.; 1989.

[7] Boyer JS, Wright SM, Porter JR. An Automated Measurement System for Characterization of RF and Gradient Coil Parameters. JMRI. 1998;8:740–747.

[8] Hoult DI, Richards RE. The signal-to-noise ratio of the nuclear magnetic resonance experiment. J Magn Reson. 1976;24:71–85.

[9] Haacke ME, Brown RW, Thompson MR, Venketesan R. Magnetic resonance imaging: Physical principles and sequence design. John Wiley & Sons Inc.; 1999.

[10] Lewitt MH. Spin Dynamics: Basics of Nuclear Magnetic Resonance. John Wiley & Sons Inc.; 2001.

[11] Gaidan DJ. NMR and its application to living systems. second edition ed. Oxford Science Publications; 1995.

[12] Hornak JP. The Basics of MRI; 2008. `http://www.cis.rit.edu/htbooks/mri/`. online.

[13] Jost G, Harting I, Heiland S. Quantitative single-voxel spectroscopy: The reciprocity principle for receive-only head coils. JMRI. 2005;21:66–71.

[14] Helms G. A precise and user-independent quantification technique for regional comparison of single volume proton MR spectroscopy of the human brain. NMR Biomed. 2000;13:398–406.

[15] Solectro AB, Product documentation: flatbed robot; 2006. CD.

[16] Anderson D, Smith L. Application Note 95-1, S-parameter techniques; 2000. `http://contact.tm.agilent.com/data/static/downloads/eng/Notes/interactive/an-95-1/an-95-1.pdf`. online.

[17] Langer-EMV Product overview; 2007. `http://www.langer-emv.de/product_en.htm`. online.

[18] Weisstein EW. Line-Plane Intersection; 2008. `http://mathworld.wolfram.com/Line-PlaneIntersection.html`. online.

[19] Eggert DW, Lorusso A, Fisher RB. Estimating 3D rigid body transformations: a comparison of four major algorithms. Machine Vision and Applications. 1997;9:272–290.

[20] Wen G, Wang Z, Xia S, Zhu D. Least-squares fitting of multiple M-dimensional point sets. Visual Comput. 2006;22:387–398.

Appendix A

S-parameters

S-parameters are used in the two-port theory and describe completely properties of a two-port system. Their advantage in microwave area is that they are simple, analytically convenient and quite easily measured. Moreover, once the parameters are determined, the behavior of the network can be predicted in any environment [7]. However, one must keep on mind that S-parameters always represent linear behavior of the system. The signal flow for an ideal two-port network is depicted in figure A.1.
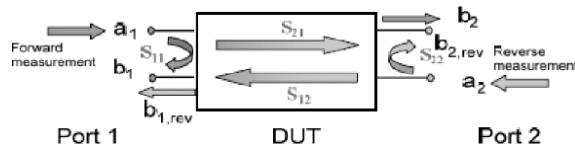
Figure A.1: Two-port network signal flow

The S-parameters are defined by the scattering matrix in equation (A.1), which links the incident waves a_1 and a_2 to the outgoing waves b_1 and b_2 [7]

$$\begin{pmatrix} b_1 \\ b_2 \end{pmatrix} = \begin{pmatrix} S_{11} S_{12} \\ S_{21} S_{22} \end{pmatrix} \begin{pmatrix} a_1 \\ a_2 \end{pmatrix} \tag{A.1}$$

The interpretation of scattering parameters is as follows [8]

S_{11}: input reflection coefficient; defined as a ratio between b_1 and a_1

S_{21}: forward transmission coefficient; defined as a ratio between b_2 and a_1

S_{12}: reverse transmission coefficient; defined as a ratio between b_1 and a_2

S_{22}: output reflection coefficient; defined as a ratio between b_2 and a_2

Appendix B

Coordinate system definition

Let the MR scanner coordinates be defined such as that the z_{sc} axis is in the direction from feet-to-head (CC/FH), let x_{sc} axis be in the left-right (LR) direction and y_{sc} axis in the anterior posterior (AP). We assume the patient lying in supine position head first in the scanner. However, note that the convention is based on external viewer's point of view, not patients!

Let the imaging voxel coordinate system be defined in the same way with its axis x_{im}, y_{im}, y_{im} pointing in the same direction as the scanner coordinates x_{sc}, y_{sc}, z_{sc} when the voxel is not rotated. Spectrum voxel coordinate system is described by axis x_{sp}, y_{sp}, z_{sp}. The situation is shown in detail in figure 3.11.

B.1 Initializing the .par and .spar files

The geometric information about imaging and spectroscopy voxels (i.e. position relative to scanner isocenter) are obtained from corresponding .par and .spar files as *offset* parameters. These are described by the Euler angles and translations. Because (if unrotated) the image coordinate system coincides with scanner coordinate system we can write

$$x_{im,offset} = \text{lr\_offset} \tag{B.1}$$

$$y_{im,offset} = \text{ap\_offset} \tag{B.2}$$

$$z_{im,offset} = \text{cc\_offset} \tag{B.3}$$

The Euler angles are defined by equations

$$x_{im,ang} = \text{lr\_angulation} \tag{B.4}$$

$$y_{im,ang} = \text{ap\_angulation} \tag{B.5}$$

$$z_{im,ang} = \text{cc\_angulation} \tag{B.6}$$

Since version 2.5.3 of the scanner software, the spectrum voxel offset is defined similarly to the image voxel. Thus, the offsets are defined by

$$x_{sp,offset} = \text{lr\_offset} \tag{B.7}$$

$$y_{sp,offset} = \text{ap\_offset} \tag{B.8}$$

$$z_{sp,offset} = \text{cc\_offset} \tag{B.9}$$

The Euler angles describing rotations are defined in the same way as in the scanner coordinate system and hence

$$x_{sp,ang} = \text{lr\_angulation} \tag{B.10}$$

$$y_{sp,ang} = \text{ap\_angulation} \tag{B.11}$$

$$z_{sp,ang} = \text{cc\_angulation} \tag{B.12}$$

To speed up the rotation and intersection functions, only coordinates of voxel vertices are used for the computations. Each voxel is formed by eight vertices — as displayed in figure B.1; the right-handed coordinate system is shown, and each of the vertices is assigned an unique number.
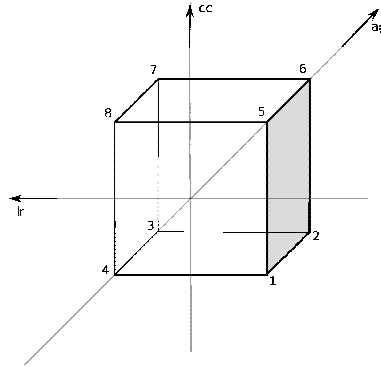
Figure B.1: Definition of coordinate system and vertices

Voxel coordinates can then be written in a matrix form:

$$\mathbf{X}_{im} = \begin{bmatrix} \mathbf{x} & \mathbf{y} & \mathbf{z} & \mathbf{1} \end{bmatrix} = \begin{bmatrix} x_1 & y_1 & z_1 & 1 \\ x_2 & y_2 & z_2 & 1 \\ x_3 & y_3 & z_3 & 1 \\ x_4 & y_4 & z_4 & 1 \\ x_5 & y_5 & z_5 & 1 \\ x_6 & y_6 & z_6 & 1 \\ x_7 & y_7 & z_7 & 1 \\ x_8 & y_8 & z_8 & 1 \end{bmatrix} \tag{B.13}$$

Considering that the voxel center and its dimensions are known, we can use equations (B.1)–(B.12) and install into equation (B.13) to obtain following

$$\mathbf{X}_{im} = \begin{bmatrix} \mathbf{x}_{im} & \mathbf{y}_{im} & \mathbf{z}_{im} & \mathbf{1} \end{bmatrix} = \begin{bmatrix} \frac{-lr}{2} & -\frac{ap}{2} & -\frac{cc}{2} & 1 \\ \frac{lr}{2} & -\frac{ap}{2} & -\frac{cc}{2} & 1 \\ \frac{lr}{2} & \frac{ap}{2} & -\frac{cc}{2} & 1 \\ -\frac{lr}{2} & \frac{ap}{2} & -\frac{cc}{2} & 1 \\ -\frac{lr}{2} & -\frac{ap}{2} & \frac{cc}{2} & 1 \\ \frac{lr}{2} & -\frac{ap}{2} & \frac{cc}{2} & 1 \\ \frac{lr}{2} & \frac{ap}{2} & \frac{cc}{2} & 1 \\ -\frac{lr}{2} & \frac{ap}{2} & \frac{cc}{2} & 1 \end{bmatrix} \tag{B.14}$$

where column **1** serves as a homogenous factor to allow multiplication with matrixes of dimension four. A correction for nonzero pixel width/height is performed later.

Appendix C

Offset parameter definition

During the work on the thesis the definition of offsets of spectral data on the Philips MR scanner system has changed twice. Because of this, it was necessary to implement checks in programmed MATLAB$^\circledR$ functions, so that they always use the correct definition and/or rotation order. Following table summarizes necessary changes.

Software version	2.1.3	2.5.1	2.5.3
Rotation order	$\mathbf{X}_{sp} = \mathbf{R}_z \mathbf{R}_x \mathbf{R}_y \mathbf{T}$	$\mathbf{X}_{sp} = \mathbf{R}_z \mathbf{R}_y \mathbf{R}_x \mathbf{T}$	$\mathbf{X}_{sp} = \mathbf{R}_z \mathbf{R}_y \mathbf{R}_x \mathbf{T}$
$\mathbf{X}_{sp,offset}$	-ap_offset	-ap_offset	ap_offset
$\mathbf{Y}_{sp,offset}$	-lr_offset	-lr_offset	lr_offset
$\mathbf{Z}_{sp,offset}$	cc_offset	cc_offset	cc_offset
$\mathbf{X}_{sp,ang}$	-ap_angulation	ap_angulation	ap_angulation
$\mathbf{Y}_{sp,ang}$	-lr_angulation	lr_angulation	lr_angulation
$\mathbf{Z}_{sp,ang}$	cc_angulation	cc_angulation	cc_angulation

Table C.1: Version difference summary; all data prior to version 2.1.3 are considered to use the same convention